CHEMISTRY OF MATERIALS

pubs.acs.org/cm

Article

The Role of the Reducible Dopant in Solid Electrolyte–Lithium Metal Interfaces

Published as part of the Virtual Special Issue "John Goodenough at 100".

Innes McClelland,▽ Hany El-Shinawi,▽ Samuel G. Booth, Anna Regoutz, Jasmin Clough, Sebastian Altus, Edmund J. Cussen, Peter J. Baker, and Serena A. Cussen*

Cite This: *Chem. Mater.* 2022, 34, 5054–5064

Read Online

ACCESS | Metrics & More | Article Recommendations | Supporting Information

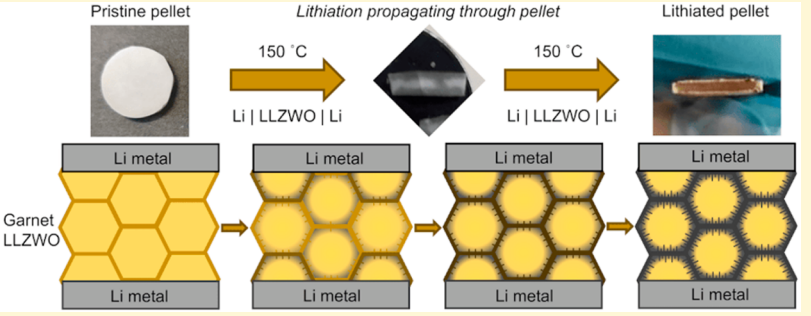

ABSTRACT: Garnet solid electrolytes, of the form $Li_7La_3Zr_2O_{12}$ (LLZO), remain an enticing prospect for solid-state batteries owing to their chemical and electrochemical stability in contact with metallic lithium. Dopants, often employed to stabilize the fast ion conducting cubic garnet phase, typically have no effect on the chemical stability of LLZO in contact with Li metal but have been found recently to impact the properties of the Li/garnet interface. For dopants more "reducible" than Zr (e.g., Nb and Ti), contradictory reports of either raised or reduced Li/garnet interfacial resistances have been attributed to the dopant. Here, we investigate the Li/LLZO interface in W-doped $Li_7La_3Zr_2O_{12}$ (LLZWO) to determine the influence of a "reducible" dopant on the electrochemical properties of the Li/garnet interface. Single-phase LLZWO is synthesized by a new sol–gel approach and densified by spark plasma sintering. Interrogating the resulting Li/LLZWO interface/interphase by impedance, muon spin relaxation and X-ray absorption spectroscopies uncover the significant impact of surface lithiation on electrochemical performance. Upon initial contact, an interfacial reaction occurs between LLZWO and Li metal, leading to the reduction of surface W^{6+} centers and an initial reduction of the Li/garnet interfacial resistance. Propagation of this surface reaction, driven by the high mobility of Li^+ ions through the grain surfaces, thickens the resistive interphases throughout the material and impedes Li^+ ion transport between the grains. The resulting high resistance accumulating in the system impedes cycling at high current densities. These insights shed light on the nature of lithiated interfaces in garnet solid electrolytes containing a reducible dopant where high Li^+ ion mobility and the reducible nature of the dopant can significantly affect electrochemical performance.

INTRODUCTION

Doped garnet-structured ceramics such as $Li_7La_3Zr_2O_{12}$ (LLZO) are among the most attractive commercial candidates for solid electrolyte materials. LLZO demonstrates high ionic conductivities (up to 1 mS cm^{-1}[11]), a large shear modulus (60 GPa[2]), and stability over a wide voltage window.[3] Doped garnet electrolytes may be accessed through traditional synthetic routes[4−8] and processed to high relative densities (>95%) via techniques such as hot-pressing[9] and spark plasma sintering.[10−13]

Undoped LLZO has a tetragonal symmetry characterized by Li^+ ion ordering and limited ion mobility.[14] Conventionally, dopants are employed to disrupt this ordering, generating isotropic three-dimensional diffusion pathways by stabilizing the cubic phase.[15,16] Dopant elements employed thus far include, but are not limited to, Ca^{2+},[17] $Fe^{2+/3+}$,[18] Al^{3+},[19,20] Ga^{3+},[5] Y^{3+},[21] Si^{4+},[22] Gd^{4+},[23] Ge^{4+},[24] Nb^{5+},[25−27] Ta^{5+},[28,29] Sb^{5+},[30,31] W^{6+},[7,32] and Te^{6+}.[33] The choice of dopant has crucial influence over the resulting garnet properties: elements such as Zn^{2+}, Al^{3+}, and Ga^{3+} preferentially substitute for Li^+; Ti^{4+}, Ge^{4+},

Received: February 5, 2022
Revised: April 24, 2022
Published: May 25, 2022

and Ta^{5+} show a tendency to occupy the Zr^{4+} site; Ca^{2+}, Y^{3+}, and Nd^{3+} are most stable when on the La^{3+} site.[34]

Even when immersed in molten lithium at 300 °C for prolonged periods, doped LLZO-based solid electrolytes retain their cubic garnet structure.[35] Recently, it has been suggested that doped-LLZO surfaces undergo structural modifications when in contact with Li. These include the possible formation of an ultrathin oxygen-deficient interphase layer,[36] or a tetragonal-like LLZO interphase,[37] due to reduction of Zr (and/or the dopant element) which is charge balanced by additional incorporation of Li^+ ions.[38] LLZO phases doped with species more prone to reduction than Zr^{4+} (e.g., Nb^{5+}, Fe^{3+}, Ti^{4+}) undergo discoloration in contact with Li metal, often indicating the formation of a reduced interphase.[35,39−41] The nature of the reducible dopant significantly influences the properties of any emergent interphase.[42,43] For example, in the case of Nb-doped LLZO, experimental observations are consistent with the formation of an oxygen-deficient interphase region while DFT calculations suggest the segregation of reduced Nb species to the LLZO surface.[36] Such processes are often associated with significant interfacial impedances which increase over time.[36,40,44] Selective doping of LLZO also affords an opportunity to fine-tune the properties of the surface. In one such example, Zhu et al.[41] report increased wettability of a Ti-doped LLZO system by Li metal due to the emergence of a reduced interphase containing Ti^{4+}/Ti^{3+}, resulting in lower interfacial impedances. They suggest the surface reaction between Ti−LLZO and Li metal enhances the wettability in a manner similar to alloy-formation or intercalation reactions in Li/LLZWO systems modified by metal[45−48] or graphite[49,50] surface layers, respectively.

Detailed study of these phenomena is often challenging due to the thin and buried nature of the interphases. Here we demonstrate the muon spin relaxation (μSR) method as a noninvasive, nondestructive, and bulk sensitive technique to directly study the Li/LLZO interphase where we apply W^{6+} as the reducible dopant (LLZWO). Guided by impedance spectroscopy (EIS), μSR affords a unique insight into ionic dynamics and structural properties in the Li/LLZWO interphase, which can be extrapolated to other Li/LLZMO systems where M is a reducible dopant.

EXPERIMENTAL SECTION

Synthesis and SPS. A sol−gel approach was used to prepare $Li_{7-x}La_3Zr_{2-x}W_xO_{12}$ with x = 0.4. Lithium acetate (Sigma-Aldrich, 99.95%), lanthanum oxide (Alfa Aesar, 99.99%, predried), zirconium oxynitrate hydrate (Sigma-Aldrich, 99.99%), and ammonium tungsten oxide hydrate (Alfa Aesar, 99.999%) were used as starting materials. Ten percent excess lithium acetate was included to compensate for losses during sintering. Stoichiometric quantities of reagents were dissolved in nitric acid and water under constant mixing. The solvents were evaporated to form a gel, which was burnt, collected, ground, and then heated at 550 °C to remove organic carbon residues. The resultant powder was pressed at 1.5 ton in a uniaxial hydraulic press and presintered at 900 °C for 6 h. Spark plasma sintering (SPS) experiments were performed using methodology identical to that of a previous study from our group,[51] with sintering conditions of 50 °C/min heating rate, 1090 °C, 10 min dwell and then cooling.

Characterization and Cell Assembly. X-ray diffraction data were collected using a Rigaku Miniflex with a Cu Kα X-ray source. Density values were obtained via helium gas displacement pycnometry using a Micromeritics AccuPyc II 1340. SEM images and EDS experiments were conducted using an FEI Inspect F50 high resolution electron microscope. For EIS and DC polarization measurements, Li^+ blocking gold electrodes were applied. For galvanostatic cycling, pellets were sandwiched between two Li foils (Sigma-Aldrich, 0.38 mm), pressed at 100 kg, and assembled within a Swagelok cell in an Ar-filled glovebox. Lithium foil was scraped using a stainless-steel blade to ensure optimal contact and a clean surface. AC impedance and galvanostatic cycling measurements were performed using a Biologic VMP-300 potentiostat. To produce "lithiated" pellets, cells were prepared identically as for galvanostatic cycling measurements, followed by a heat treatment at 150 °C. Origin was used to create all graphs shown, while VESTA was used to design unit cell depictions.[52]

Muon Spin Relaxation. Muon measurements were completed on the EMU spectrometer at the ISIS Neutron and Muon Source. Temperature-dependent measurements were taken between 150 K and 400 K, whereby spin polarized, positively charged muons were implanted into both pristine and lithiated LLZWO pellets to act as a local probe of nearby fluctuating magnetic moments. Longitudinal field measurements of 0, 5, and 10 G were applied alongside 100 G transverse field runs at each temperature. A custom steel cell was used to contain sample pellets, which were polished to around 1.1 mm thick to ensure adequate muon implantation. Any muons not incident on the inspection window were stopped by the silver mask; any consequent signal was subtracted as background. All data analysis was completed using Mantid.[53]

X-ray Absorption Spectroscopy and X-ray Photoelectron Spectroscopy. X-ray absorption spectroscopy (XAS) measurements were performed at the B18 XAS beamline at Diamond Light Source. Measurements were conducted on the W L_3 edge in transmission mode. Samples were mixed thoroughly with cellulose in appropriate quantities and pressed at 500 kg into 13 mm diameter pellets. Pellets were loaded into a rack using Kapton tape and heat sealed in an Al bag under an Ar atmosphere. Data analysis was completed using the Demeter software package.[54]

X-ray photoelectron spectroscopy (XPS) experiments were performed on a Thermo Scientific K-Alpha+ X-ray photoelectron spectrometer, which incorporates a monochromated, microfocused Al Kα X-ray source ($\hbar\nu$ = 1486.7 eV) and a 180° double focusing hemispherical analyzer with a 2D detector. Data were collected at 200 eV pass energy for survey and 20 eV pass energy for core level spectra using an X-ray spot size of 400 μm. All data were analyzed using the Avantage software package.

RESULTS AND DISCUSSION

Dense ceramics of single-phase W-doped LLZO ($Li_{6.2}La_3Zr_{1.6}W_{0.4}O_{12}$: hereafter referred to as LLZWO) were successfully achieved via sol−gel synthesis followed by spark plasma sintering (SPS). A small impurity (~1.5 wt %) of Li_6WO_6 was observed in the as-synthesized material but was subsequently not distinguishable by X-ray diffraction upon SPS treatment. Figure 1(a) shows X-ray diffraction patterns of an as-synthesized sample and a sample post-SPS treatment. The material crystallizes in a cubic garnet structure (Figure 1(b)) with a refined unit cell parameter of a = 12.9294 (4) Å, determined by a Rietveld fit to the diffraction data (shown in Figure S2). SPS-processed samples possessed relative densities of 94% (Figure 1(c)). EDX mapping through a cross-section of the garnet pellet (Figure 1(d)) revealed a homogeneous distribution of tungsten within the material, consistent with the incorporation of tungsten in the cubic garnet lattice as indicated by X-ray diffraction.[1]

Impedance spectroscopy measurements on LLZWO using blocking gold electrodes revealed a room temperature conductivity of 3×10^{-4} S cm^{-1}, and an activation energy for Li^+ transport (E_a) of 0.403 eV in the temperature range 0−120 °C. The impedance plot collected at 0 °C is shown in Figure 2(a). Fitting to these data was performed using the equivalent circuit $[R_1Q_1][R_2Q_2][R_3Q_3][Q_4]$, where [RQ] is a resistor (R) in parallel with a constant phase element [Q]. The

https://doi.org/10.1021/acs.chemmater.2c00379
Chem. Mater. 2022, 34, 5054−5064

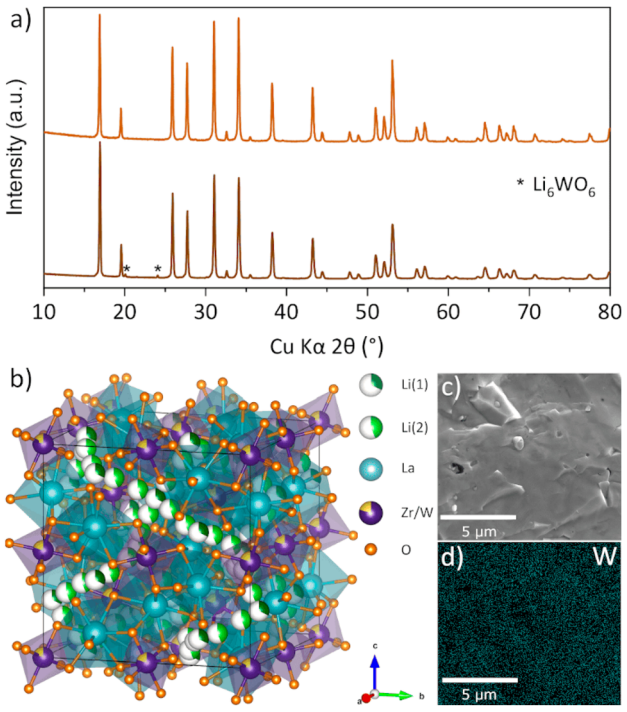

Figure 1. (a) X-ray diffraction patterns of sol−gel-synthesized (bottom) and SPS-treated (top) $Li_{6.2}La_3Zr_{1.6}W_{0.4}O_{12}$. A small 1.5 wt % Li_6WO_6 impurity phase present in the as-synthesized pattern is removed after SPS processing. (b) Unit cell diagram of LLZWO. Li(1) (24d) is light green and tetrahedrally coordinated, and Li(2) (96h) is dark green and octahedrally coordinated, while both have a white vacancy fraction. La is turquoise and forms a LaO_8 dodecahedron, and Zr/W is purple/yellow and forms a $[Zr/W]O_6$ octahedron.[27] (c) Cross-sectional SEM image of an SPS pellet and (d) EDS image revealing uniform tungsten dispersion across the sample.

semicircle observed at high frequencies ($[R_1Q_1]$) represents the total resistance of the material, with a capacitance, calculated from the fit parameter (Q), of 5×10^{-11} F. The features observed at intermediate/low frequencies ($[R_2Q_2]$-$[R_3Q_3]$) possess refined capacitances in the range of 1×10^{-6} F and therefore likely represent surface/interfacial effects.[55,56] These features lose/gain definition at higher temperatures (Figure S5), complicating the fitting process. A detailed analysis of these features is omitted from this work.

To investigate the contribution of electronic conductivity to the total conductivity of LLZWO, a DC polarization measurement was performed between 0.6 and 1.2 V in 0.3 V steps (Figure S7) which estimated a partial electronic conductivity of 5 (1) $\times 10^{-10}$ S cm^{-1}. This value is several orders of magnitude lower than conductivity measured using EIS, which suggests a very low contribution from electronic conductivity in the pure material. To examine the effect of tungsten doping on the "reducibility" of LLZO, a 70:30 wt % mixture of LLZWO and conductive carbon (LLZWO/C) was assembled in a half-cell using Li metal as the counter electrode and 1 M $LiPF_6$ (in 1:1 EC/DMC) as a liquid electrolyte. A similar cell containing Ta-doped LLZO (LLZTO/C) was assembled for comparison. The redox stability of Ta-doped garnets is well-documented,[36,39] and this comparison allows us to rule out the consumption of Li^+ in the buildup of the solid−electrolyte interface. Figure S8 shows identical discharge profiles of the two half-cells, indicating that there is no difference in redox activities. Hence, unlike the W-containing garnet compound $Li_3Nd_3W_2O_{12}$,[57−59] Li^+ is not simply intercalated into LLZWO/C in the presence of a Li^+ liquid electrolyte. This is consistent with the low observed electronic conductivity.

In contact with Li metal, LLZWO surfaces undergo faint coloration to a yellowish-brown color (Figure 2(b)). This turns to a deep brown/black color upon mild heating to temperatures as low as 80 °C, indicating a surface reaction that occurs between LLZWO and metallic lithium. This reaction likely involves the incorporation of Li^+ into the surface grains, associated with the reduction of W^{6+} centers on the surface (confirmed later by XAS). Wolfstein et al. reported chemical coloration of LLZO after heating with Li metal at elevated temperatures, assigning this to the formation of color centers due to electrons trapped at oxygen vacancy sites.[35] Coloration in contact with Li metal is also reported in garnets containing Fe and Nb and was attributed to the reduction of these elements to lower oxidation states.[36,39,40,43] Coloration in these systems often disappears after a short heat treatment in an oxidizing atmosphere, which is also observed for our LLZWO (Figure S9).

To investigate the electrochemical properties of the Li/LLZWO interface, symmetric Li/LLZWO/Li cells were constructed and tested at 80 °C. A time-resolved impedance study is shown in Figure 2(c). The spectra reveal a high-frequency semicircle which agrees well with the total resistance of the pellet measured using gold blocking electrodes (Figure S5) and a second semicircle at lower frequency characteristic of Li^+ transport at the Li/LLZWO interface. A significant drop in the interfacial resistance is observed with time, reaching a stable value after 24 h. Hence, under the employed cell preparation and testing conditions, the Li/LLZWO surface reaction supports low interfacial resistances, likely through enhancement of the garnet surface's wettability by Li with the aid of elevated temperatures.[60] This is consistent with recent observations of garnet systems containing Ti as the reducible element[41] and also agrees well with the improved wettability accessible through other surface reactions, such as alloy-formation or Li^+-intercalation in Li/M/garnet or Li/C/garnet systems, respectively.[46−49]

To further study the stability of the Li/LLZWO interface during Li-stripping and deposition, symmetric Li/LLZWO/Li cells were cycled at 250 μA cm^{-2} at 80 °C (Figure 2(d)). A small increase in cell resistance (voltage) is observed within 20 h of cycling, which rose notably as the current density was increased to 500 μA cm^{-2}. The pellet resistance then grows rapidly after cycling at 500 μA cm^{-2} for more than 8 h. Interestingly, after the galvanostatic cycling experiment, the brown/black color characteristic of the Li/LLZWO interface had deeply propagated across the pellet (Figure 3(a)) and is coupled by a noticeable loss in mechanical properties. Despite the importance of the formation of the Li/LLZWO interface to ensure good contact between Li and LLZWO (as shown in Figure 2(c)), the propagation of the surface reaction through the pellet upon cycling adds a large resistance to the system. This propagation is clearly driven by the high mobility of Li^+ through the pellet under the experimental conditions applied.

We assumed that this highly dynamic state of Li^+ can also be achieved by heating a Li/LLZWO/Li cell at a relatively high temperature (<melting point of Li) in the absence of electric potential. Interestingly, when a Li/LLZWO/Li cell was heated

https://doi.org/10.1021/acs.chemmater.2c00379
Chem. Mater. 2022, 34, 5054−5064

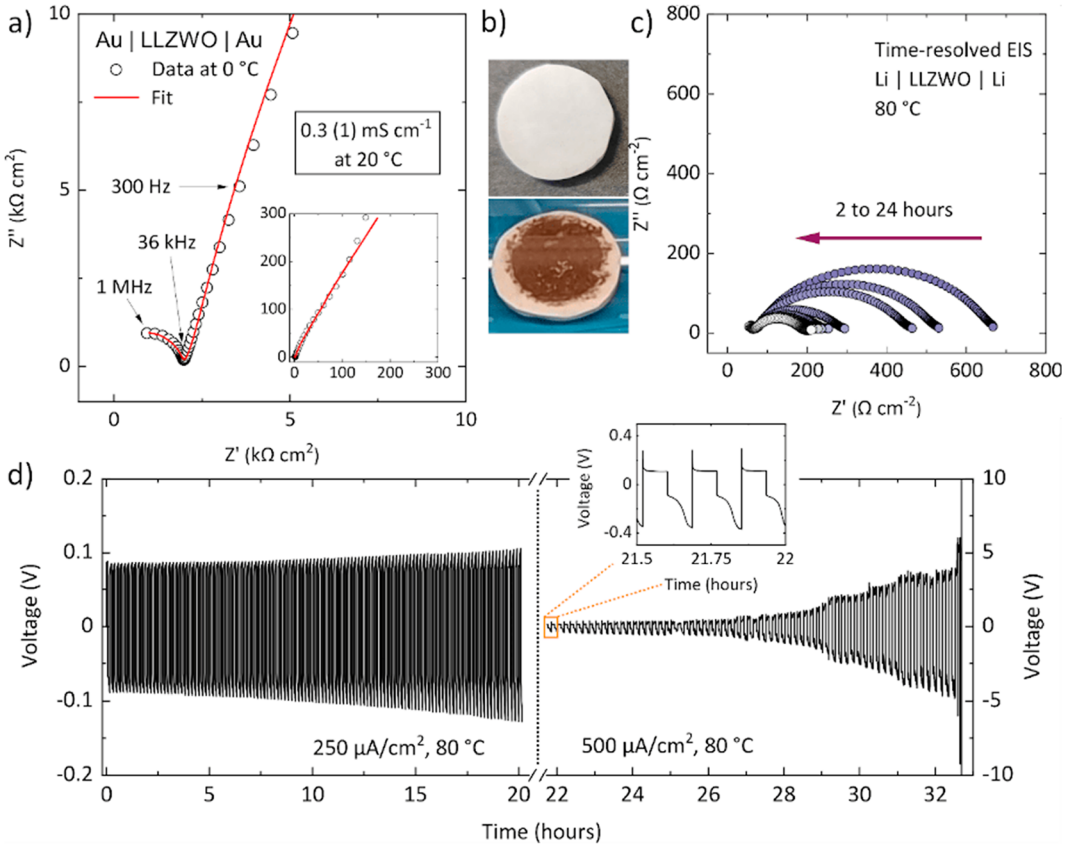

Figure 2. (a) Impedance spectroscopy measurement of LLZWO at 0 °C with blocking Au electrodes, fitted using an $[R_1Q_1][R_2Q_2][R_3Q_3][Q_4]$ equivalent circuit. (b) A pristine LLZWO pellet (upper), and the same pellet with brown coloration upon interfacial reaction with metallic Li (lower). (c) Time-resolved impedance experiment in a symmetric cell with Li electrodes at 80 °C. The interfacial resistance decreases over time before reaching a minimum. The bulk resistance (represented by a small semicircle at high frequency) remains constant. (d) Galvanostatic cycling profile at 80 °C of a Li/LLZWO/Li cell at 250 and 500 μA cm^{-2}. The electrolyte is stable at 250 μA cm^{-2}, but its resistance begins to grow upon application of 500 μA cm^{-2} before short-circuiting at 33 h. Inhomogeneous Li stripping/plating is observed (inset).

at 150 °C in the absence of an external electric field, we observed a propagation of the coloration through the LLZWO pellet to an extent dependent on the heating time. To correlate this process with the buildup of the resistance during galvanostatic cycling, we heated a freshly prepared symmetric Li/LLZWO/Li cell at 150 °C for set time periods (2, 24, 48, and 96 h) and measured the room temperature impedance of the cell afterward. By the end of the experiment, we observed coloration across the whole pellet (Figure 3(a)). X-ray diffraction data collected from the reacted pellet after lithiation reveal that the material preserves the cubic garnet phase (Figure S11).

Figure 3(b) shows the impedance spectra collected from the cell after each heat treatment. The initial impedance of the cell (RT; no heating) is nicely fitted using two [RQ] equivalent circuit components ($[R_1Q_1][R_2Q_2]$), corresponding to the total resistance of the pellet and the interfacial resistance. The total resistance here refers to the resistance within the grains (bulk resistance) and in-between the grains (grain-boundary resistance) and agrees well with the total LLZWO pellet resistance measured using gold blocking electrodes. After 2 h heating at 150 °C, there is an initial drop in interfacial resistance consistent with the formation of the Li/LLZWO interface. No change is observed in the high-frequency semicircle, indicating no effect from the interface formation (at this stage) on either the bulk or grain-boundary resistances. Upon further heating at 150 °C (for 24, 48, and 96 h), a reduction in size of the high-frequency semicircle and a gradual increase of the low-frequency semicircle were observed. The resistance associated with the high-frequency semicircle was approximately half of the initial (bulk + gain-boundary) resistance and is constant in the three spectra (at 24, 48, and 96 h).

The three spectra were fitted using $[R_1Q_1][R_2Q_2][R_3Q_3]$ equivalent circuits, where two [RQ] terms were required to fit the low-frequency semicircle due to the growth of the interphase (see Figure S12 and Table S3 for the fitting results). For the three spectra, the capacitance associated with high-frequency semicircle is of the order of 10^{-11}–10^{-12} F, while the capacitance associated with the low-frequency semicircle is $\sim 10^{-9}$ F. The former capacitance value clearly reflects a contribution from the bulk resistance.[55] These results indicate that the grain-boundary contribution to the resistance has been separated from the bulk resistance, suggesting that the diffusion processes within these areas now occur at different time scales. The evolution of a new component of the interfacial resistance indicates that the Li^+ transport between the grains likely occurs through modified, more resistive interfaces, which can be linked to the propagation of the Li/LLZWO interphase through the pellet. This is schematically represented in Figure 3(a).

https://doi.org/10.1021/acs.chemmater.2c00379
Chem. Mater. 2022, 34, 5054−5064

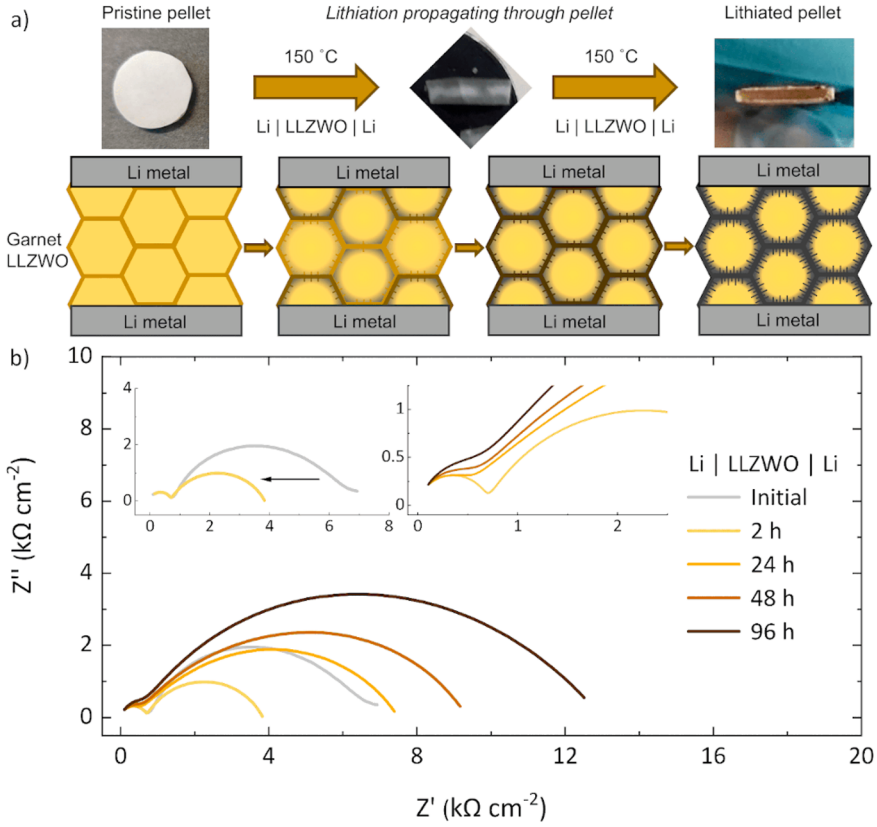

Figure 3. (a) Schematic outlining the procession of an interfacial reaction between Li metal and garnet LLZWO. The lithium/LLZWO interfacial reaction is predicted to propagate through the grain surfaces of the material. This reaction can be accelerated via elevated temperature or via application of an electric field gradient: the former is employed in this study to produce a "lithiated" LLZWO sample, which undergoes a color change from white/gray to brown/black throughout the pellet. (b) Experiment wherein a symmetric Li/LLZWO/Li cell was heated to 150 °C for varying time periods and cooled to room temperature and the impedance spectrum measured. Only the spectra fits are shown here; data with fits are shown in Figure S12. The insets in panel b show the magnification of the spectra corresponding to (i) the initial reduction of the interfacial resistance (upper left) and (ii) the reduction of the resistance of the pellet due to separation of bulk and grain-boundary resistances (upper right).

In this model, a surface modification (we refer to as "lithiation" henceforth) of the grains is proposed to describe the interface propagation in LLZWO. In the proposed mechanism, Li^+ is picked up by the W^{6+} centers to drive the surface lithiation of the grains. As shown in Figure 3(a), contact between Li metal and LLZWO initiates a lithiation of the surface grains which promotes good contact between Li metal and LLZWO and leads to an initial drop of the interfacial resistance (also seen in Figure 2(c)). However, upon full propagation of this surface reaction through the pellet, Li^+ transport between grains is forced to pass through lithiated interfaces, which appear more resistive than the pristine interfaces, and consequently result in an overall buildup of the resistance. It is expected that volume changes associated with the lithiation of the grain surfaces will lead to partial loss of the particle−particle contact (Figure S10) and will contribute to the buildup of the resistance (which accounts for the brittleness of lithiated pellets). To validate the model in Figure 3(a), and to confirm the formation of resistive interphases in Li/LLZWO systems, a "lithiated" LLZWO sample was produced from heating a Li/LLWZO/Li cell and investigated by muon spin relaxation (μSR), XAS, and XPS.

μSR can be applied as a volume-averaged, nondestructive probe to investigate the Li^+ dynamics and internal characteristics[61,62] of LLZWO before and after lithiation. Longitudinal and transverse fields were applied in the temperature range 150−400 K: the fitting procedures are described in the Supporting Information (eqs S1−S4), while plots of fitted data at 317 K are shown in Figure 4. Transverse field runs were conducted at 100 G, much higher than the expected internal nuclear field distribution, and thus almost all muon spins are expected to precess in the direction of the applied field. Visually, the pristine sample displays an expected behavior for a lithium-ion conductor;[63] there is a small relaxation in the envelope of the asymmetry signal likely due to the motion of Li^+ ions. Conversely, the lithiated sample appears to show multiple beating frequencies, indicating two distinct contributions to the signal. Consequently, pristine LLZWO was found to model well to one Gaussian oscillation function (eq S1), whereas postlithiation two oscillation functions were required (eq S2).

The distinct signals in lithiated LLZWO, displayed in Table 1, can be roughly correlated to the bulk and surface regions of the grains, respectively (see Figure 3(a) for a visual interpretation). Muon implantation is volume-averaged (and dependent on density): the signal amplitudes therefore represent the relative volume fraction of each muon environment. Only one symmetrically equivalent oxygen site is known for garnet materials,[64] and lithiated LLZWO was confirmed as garnet phase by X-ray diffraction (Figure S11), which suggests that the dual signal arises from two magnetically distinct volumes rather than two discrete stopping sites with

https://doi.org/10.1021/acs.chemmater.2c00379
Chem. Mater. 2022, 34, 5054−5064

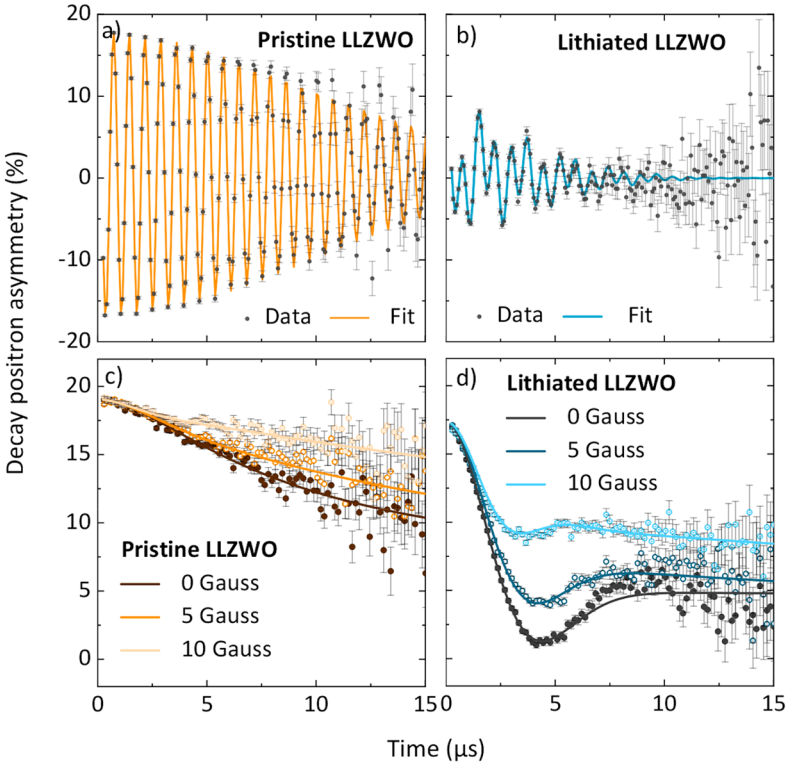

Figure 4. Fitted μSR measurements at 317 K of (a) pristine LLZWO in a 100 G transverse field, (b) lithiated LLZWO in a 100 G transverse field, (c) pristine LLZWO in 0, 5, and 10 G applied longitudinal fields, and (d) lithiated LLZWO in 0, 5, and 10 G applied longitudinal fields. The data show highly modified behavior after LLZWO lithiation, with two precession frequencies visualized in panel b and a quasi-static Li^+ environment evident in panel d.

Table 1. Fitting Results for a 100 G Transverse Field Measurement at 317 K

material	function	Gaussian amplitude	relaxation rate, σ (μs^{-1})	frequency (MHz)	phase, Φ	background amplitude	χ^2
pristine LLZWO	Gaussian oscillation	0.1794 (4)	0.0704 (9)	1.3939 (2)	0.035 (3)	0.0058 (2)	1.07
lithiated LLZWO	Gaussian oscillation 1	0.0463 (6)	0.283 (6)	0.564 (2)	0.26 (2)	0.0051 (3)	1.22
	Gaussian oscillation 2	0.0711 (5)	0.159 (3)	1.350 (7)	−0.041 (9)		

independent magnetic distributions within the unit cell.[65] The amplitudes do not change significantly with temperature (Figure S14), implying no significant magnetic ordering in the measured temperature region.

The muon precession frequency in Gaussian oscillation 1 (predicted as the grain surface region) is lowered from the expected Larmor precession in a 100 G applied field (~1.35 MHz), while the relaxation rate (σ) is significantly increased. The nuclear magnetic fields present[66] are insufficiently strong to produce this frequency of oscillation (0.564 MHz),[67] meaning it is likely an electronic effect. Muonium formation (μ^+e^-[68]) upon implantation is well-known for insulating and semiconducting materials[62,69] and can undergo variable strengths of hyperfine coupling. Intercalated Li^+ (linked with reduced tungsten) adds competing electron density and hence some implanted muons will not chemically bind with oxygen as expected but will instead form muonium states.[68] Muonium associated with concentrated electron centers (similar to shallow donor states[70]) in oxygen vacancies, as is postulated to cause the interphase discoloration, would have a lower hyperfine coupling energy and cause the oscillation frequency shift to 0.564 (2) MHz. Furthermore, muonium states not associated with electron centers will have a large hyperfine coupling[71] and thus will undergo a rapid spin relaxation, causing the loss of total signal amplitude observed for the lithiated sample.

To elucidate the rate of Li^+ diffusion and characteristic nuclear magnetic environment, longitudinal fields were applied. As electronic fields are generally stronger than nuclear fields, weak longitudinal fields can distinguish between the two.[72,73] A 10 G applied field was sufficient to largely decouple the nuclear dipole interaction of the muons, indicating a relatively weak characteristic nuclear magnetic environment in LLZWO. Data for pristine LLZWO were fitted using a dynamic Kubo−Toyabe function[72] (eq S3), while the evidence of a dual muon environment predicated an additional Gaussian relaxation for lithiated LLZWO (eq S4). At 317 K, pristine LLZWO exhibits a slow relaxation rate, indicating fast Li^+ dynamics. Conversely, lithiated LLZWO appears to follow the form of the static Kubo−Toyabe function, whereby a fast relaxation is followed by a return to around 1/3 of the initial asymmetry.[72] However, a gradual decrease in asymmetry at longer time scales (>8 μs) indicates the presence of dynamical Li^+, albeit at a lesser rate than observed for pristine LLZWO.

The field fluctuation rate, ν, was obtained via longitudinal field fitting and provides a direct analogy to the lithium hopping rate.[74] At low temperature, most Li^+ cannot overcome motional barriers; the onset of diffusion is observed to occur at

https://doi.org/10.1021/acs.chemmater.2c00379
Chem. Mater. 2022, 34, 5054−5064

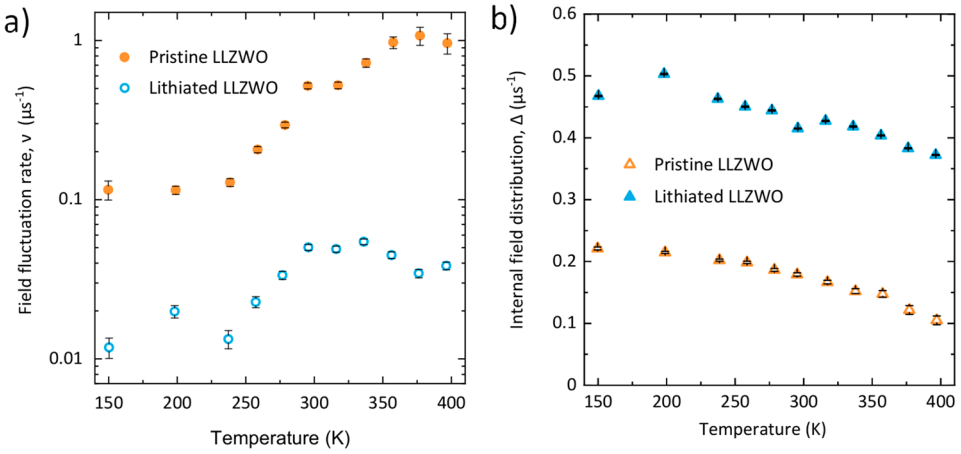

Figure 5. (a) The temperature dependence of the field fluctuation rate, ν, which is analogous to the lithium hopping rate. Lithiated LLZWO displays values of ν around 1 order of magnitude lower than pristine. (b) The temperature dependence of the static internal field distribution width. Δ is a measure of the width of the magnetic field distribution experienced by an implanted muon, governed primarily by the nuclear moment and distance of nearby nuclei. The large increase for lithiated LLZWO strongly suggests a higher Li content.

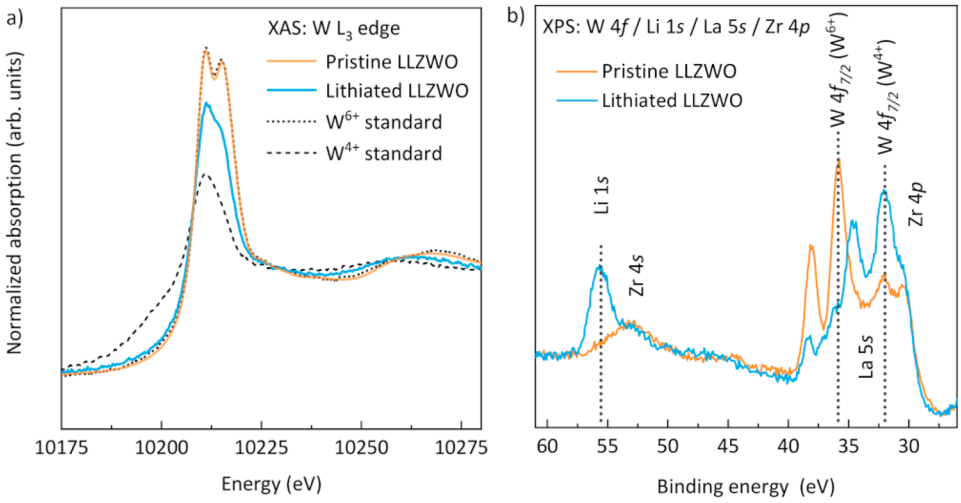

Figure 6. X-ray absorption spectroscopy (XAS) measurements of the W L_3 edge for pristine and lithiated LLZWO samples, as well as the W^{6+} standard $Li_3Nd_3W_2O_{12}$ (LNWO) and the W^{4+} standard WO_2. (b) X-ray photoelectron spectroscopy (XPS) spectrum covering the W 4f/Li 1s/La 5s/Zr 4p core level spectra. The spectra were normalized to the Zr $3d_{5/2}$ peak area for the respective samples.

around 250 K for both samples, above which ν increases exponentially. Given the crystal structure remains similar (Figure S11), ν can be compared directly. There is 1 order of magnitude difference in ν between pristine and lithiated LLZWO at room temperature (Figure 5), informing that Li^+ diffusion occurs far more rapidly prelithiation, in agreement with the formation of resistive interphases upon lithiation as found via EIS. An activation energy for Li^+ diffusion in pristine LLZWO was found via an Arrhenius analysis as 120 (3) meV, comparable to other values reported for solid electrolyte materials using μSR.[4,69] This is lower than that measured by EIS due to the relative lack of grain boundary/surface influences on muons as a local probe.

The temperature evolution of the width of the static internal field distribution (Δ), which is dependent on proximity and size of nearby nuclear dipole moments, is shown in Figure 5(b). The abundance of isotopes with significant nuclear moments is very low for Zr, W, and O (11, 14, and 0.04% for ^{91}Zr, ^{183}W, and ^{17}O, respectively); Li and La will have the greatest influence on Δ.[66] Given no structural contraction is observed (Figure S11), the large rise in Δ displayed in Figure 5(b) must be a result of the additional nuclear moments from penetrated Li which act to increase the average field distribution width felt by the muon. Dipolar field calculations indicate that increased Li occupancy alone cannot account for this large a change in Δ, and thus the increased Li content and/or reduction of tungsten likely alters the preferred muon stopping site in the grain surface region. The form of Δ is similar for both samples, indicating similar diffusion processes. The smooth decrease at higher temperatures aligns with previous reports,[4,75−77] signaling a motional narrowing effect caused by Li^+ diffusion.

The diffusion coefficient of Li^+, D_{Li}, was determined as $5.6(5) \times 10^{-11}$ cm^2 s^{-1} at 317 K for pristine LLZWO using eq S5, concurring with the fast conductivity observed via EIS, and in excellent agreement to other garnet materials studied using μSR.[4,78] A large reduction in D_{Li} after lithiation is obvious due to the direct relationship with ν and similar structural parameters. The spatial distribution of ions in the cubic symmetry of garnets permits rapid Li^+ diffusion. Thus,

https://doi.org/10.1021/acs.chemmater.2c00379
Chem. Mater. 2022, 34, 5054−5064

increased Li content rationalizes the reduction in ν, as blocked pathways hinder diffusion rates, somewhat resembling conductivity in the tetragonal phase.[16,79] Chemical reduction of W^{6+} to W^{4+} may also increase the diffusional bottleneck due to the ionic radii increase from 60 to 66 pm and lengthening of the W−O bond.[41,80] Given the inhomogeneous muon environment and uncertainty over precise Li content, it was deemed inappropriate to report a single activation energy or diffusion coefficient for lithiated LLZWO. Indeed, it suffices that the diffusion coefficient is predicted as at least 1 order of magnitude lower after lithiation. This matches well with galvanostatic cycling experiments (Figure 2(d)) which outline the resistive rise due to the propagation of the interfacial reaction. Under high applied current densities, the Li^+ diffusion coefficient is a limiting factor,[81] and thus with the propagation of Li/W reduction the resistive growth rate will increase.

To justify the predicted reduction of tungsten caused by lithiation of the grain surfaces, transmission mode X-ray absorption spectroscopy (XAS) measurements of lithiated LLZWO were collected on the W L_3 edge. Normalized absorption spectra are shown in Figure 6 for pristine and lithiated LLZWO, as well as $Li_3Nd_3W_2O_{12}$ (LNWO) as a W^{6+} standard and WO_2 as a W^{4+} standard. LNWO is a low lithium content garnet material which may be used as a low voltage insertion anode due to the well-established reducibility of W^{6+} to W^{4+} under cycling conditions below 1.0 V.[57−59] In this instance it acts as an ideal W^{6+} standard due to the reliability of W^{6+} states in the pristine form and the identical local coordination environment. This is shown experimentally in Figure 6, as LNWO precisely matches the edge position and line shape of pristine LLZWO. The split peaks observed for the W^{6+} samples are indicative of the ligand field splitting of 5d electron states, generally only distinguishable for octahedrally coordinated W units.[82] WO_2 was employed as a pure W^{4+} standard and displays a smaller, broad peak, with no splitting and a small shift in peak position to a lower energy.[83] The peak intensity of lithiated LLZWO is observed midway between the W^{6+} and W^{4+} standards, while the splitting is dampened somewhat, and a minor but clear peak shift to lower energy is evident. Hence, XAS measurements confirm that partial tungsten reduction has occurred during LLZWO lithiation, producing a mixed $W^{6+/4+}$ oxidation state.

This observation is further confirmed by X-ray photoelectron spectroscopy (XPS). Survey spectra for both samples are included in the Supporting Information and show all expected core and Auger lines. The La and Zr core level spectra (Figures S18) show only minute changes before and after lithiation and occur at binding energies commensurate with oxide environments. Figure 6(b) shows the binding energy region covering the W 4f and Li 1s core levels as well as the Zr 4s/4p and La 5s core levels. A clear increase in the Li 1s signal is observed after lithiation. In parallel, a clear change in tungsten oxidation state occurs from W^{6+} before lithiation to W^{4+} after lithiation. Although it is not possible to determine the quantitative ratio of the two oxidation states due to the complex overall spectra caused by overlap with the Zr and La core levels, the main W $4f_{7/2}$ lines provide clear evidence for the partial reduction also observed in XAS. The W 4d spectra (Figures S18) displays the same behavior as the W 4f core level and further confirms the partial reduction.

CONCLUSIONS

Investigation of buried interfaces in battery materials is a challenging prospect; here we find the LLZWO garnet an excellent candidate for studying the influence of a "reducible" dopant on the electrochemical properties of the Li/garnet interface through a combination of impedance analysis with local structural and dynamic tools. We have successfully followed the propagation of the Li/LLZWO surface reaction throughout the material where an initial decrease in the Li/garnet interfacial resistance indicates good contact between the Li metal and the LLZWO surface. This is followed by a developing large resistance as Li^+ mobility is progressively impeded. Insights from impedance spectroscopy reveal no change in the bulk resistance and a clear evolution of the grain-boundary/interfacial resistances, indicating that a modification is occurring at the grain surfaces. Muon spin relaxation reveals that two distinct environments in LLZWO exist after contact with Li, one of which is characterized by an increased electronic field component and intercalated Li, whose presence is confirmed via nuclear magnetic field distribution analysis. Meanwhile, Li^+ diffusion within this region is greatly hindered and contributes to the large resistance observed in the material after lithiation. These results propose a surface lithiation of the garnet grains that produces thick interphases easily detected by muon spectroscopy. Surface lithiation is driven by the high mobility of Li^+ in the system and is believed to occur via partial reduction of W^{6+} to W^{4+}, as evidenced by XAS and XPS. This combination of local and bulk characterization methods has uncovered the role and behavior of reducible dopants within the Li/garnet interphase, insights which are increasingly important in guiding control over these interfaces for improvements in performance.

ASSOCIATED CONTENT

Supporting Information

The Supporting Information is available free of charge at https://pubs.acs.org/doi/10.1021/acs.chemmater.2c00379.

Data fitting details for diffraction, impedance, muon, and XPS experiments along with details of imaging and experimental methodologies (PDF)

AUTHOR INFORMATION

Corresponding Author

Serena A. Cussen − *The Faraday Institution, Didcot OX11 0RA, U.K.; Department of Materials Science and Engineering, The University of Sheffield, Sheffield S1 3JD, U.K.;* orcid.org/0000-0002-9303-4220; Email: s.cussen@sheffield.ac.uk

Authors

Innes McClelland − *Department of Chemical and Biological Engineering, The University of Sheffield, Sheffield S1 3JD, U.K.; ISIS Neutron and Muon Source, Science and Technology Facilities Council, Rutherford Appleton Laboratory, Didcot OX11 0QX, U.K.; The Faraday Institution, Didcot OX11 0RA, U.K.;* orcid.org/0000-0001-9821-715X

Hany El-Shinawi − *The Faraday Institution, Didcot OX11 0RA, U.K.; Chemistry Department, Faculty of Science, Mansoura University, Mansoura 35516, Egypt*

Samuel G. Booth − *Department of Chemical and Biological Engineering, The University of Sheffield, Sheffield S1 3JD,*

https://doi.org/10.1021/acs.chemmater.2c00379
Chem. Mater. 2022, 34, 5054−5064

U.K.; The Faraday Institution, Didcot OX11 0RA, U.K.; orcid.org/0000-0001-7643-4196

Anna Regoutz − *Department of Chemistry, University College London, London WC1H 0AJ, U.K.; orcid.org/0000-0002-3747-3763*

Jasmin Clough − *The Faraday Institution, Didcot OX11 0RA, U.K.; Department of Materials Science and Engineering, The University of Sheffield, Sheffield S1 3JD, U.K.*

Sebastian Altus − *The Faraday Institution, Didcot OX11 0RA, U.K.; Department of Materials Science and Engineering, The University of Sheffield, Sheffield S1 3JD, U.K.; orcid.org/0000-0001-8433-4830*

Edmund J. Cussen − *The Faraday Institution, Didcot OX11 0RA, U.K.; Department of Materials Science and Engineering, The University of Sheffield, Sheffield S1 3JD, U.K.; orcid.org/0000-0002-2899-6888*

Peter J. Baker − *ISIS Neutron and Muon Source, Science and Technology Facilities Council, Rutherford Appleton Laboratory, Didcot OX11 0QX, U.K.; The Faraday Institution, Didcot OX11 0RA, U.K.; orcid.org/0000-0002-2306-2648*

Complete contact information is available at: https://pubs.acs.org/10.1021/acs.chemmater.2c00379

Author Contributions

▽These authors contributed equally.

Author Contributions

The manuscript was written through contributions of all authors. All authors have given approval to the final version of the manuscript.

Notes

The authors declare no competing financial interest.

■ ACKNOWLEDGMENTS

The authors thank the ISIS Neutron and Muon facility, through the award of beamtime (DOI: 10.5286/ISIS.E.RB1920550), a Facility Development Studentship for IMC, and Josef Lewis and Jamie Nutter for enabling the experiment. We also thank the Diamond Light Source for the award of beamtime as part of the Energy Materials Block Allocation Group SP14239. This work was supported by the ICSF Faraday Challenge project SOLBAT (grant FIRG007).

■ REFERENCES

(1) Thangadurai, V.; Narayanan, S.; Pinzaru, D. Garnet-type solid-state fast Li ion conductors for Li batteries: Critical review. *Chem. Soc. Rev.* **2014**, *43*, 4714−4727.

(2) Pasta, M.; Armstrong, D.; Brown, Z. L.; Bu, J.; Castell, M. R.; Chen, P.; Cocks, A.; Corr, S. A.; Cussen, E. J.; Darnbrough, E.; Deshpande, V.; Doerrer, C.; Dyer, M. S.; El-Shinawi, H.; Fleck, N.; Grant, P.; Gregory, G. L.; Grovenor, C.; Hardwick, L. J.; Irvine, J. T. S.; Lee, H. J.; Li, G.; Liberti, E.; McClelland, I.; Monroe, C.; Nellist, P. D.; Shearing, P. R.; Shoko, E.; Song, W.; Jolly, D. S.; Thomas, C. I.; Turrell, S. J.; Vestli, M.; Williams, C. K.; Zhou, Y.; Bruce, P. G. 2020 roadmap on solid-state batteries. *J. Phys. Energy* **2020**, *2*, 032008.

(3) Schwietert, T. K.; Arszelewska, V. A.; Wang, C.; Yu, C.; Vasileiadis, A.; de Klerk, N. J. J.; Hageman, J.; Hupfer, T.; Kerkamm, I.; Xu, Y.; van der Maas, E.; Kelder, E. M.; Ganapathy, S.; Wagemaker, M. Clarifying the relationship between redox activity and electrochemical stability in solid electrolytes. *Nat. Mater.* **2020**, *19*, 428−435.

(4) Amores, M.; Ashton, T. E.; Baker, P. J.; Cussen, E. J.; Corr, S. A. Fast microwave-assisted synthesis of Li-stuffed garnets and insights into Li diffusion from muon spin spectroscopy. *J. Mater. Chem. A* **2016**, *4*, 1729−1736.

(5) Howard, M. A.; Clemens, O.; Kendrick, E.; Knight, K. S.; Apperley, D. C.; Anderson, P. A.; Slater, P. R. Effect of Ga incorporation and Li ion conductivity of $La_3Zr_2Li_7O_{12}$. *Dalton Trans.* **2012**, *41*, 12048.

(6) Hu, Z.; Liu, H.; Ruan, H.; Hu, R.; Su, Y.; Zhang, L. High Li-ion conductivity of Al-doped $Li_7La_3Zr_2O_{12}$ synthesized by solid-state reaction. *Ceram. Int.* **2016**, *42*, 12156−12160.

(7) Li, Y.; Wang, Z.; Cao, Y.; Du, F.; Chen, C.; Cui, Z.; Guo, X. W-Doped $Li_7La_3Zr_2O_{12}$ Ceramic Electrolytes for Solid State Li-ion Batteries. *Electrochim. Acta* **2015**, *180*, 37−42.

(8) Liu, Q.; Geng, Z.; Han, C.; Fu, Y.; Li, S.; He, Y.; Kang, F.; Li, B. Challenges and perspectives of garnet solid electrolytes for all solid-state lithium batteries. *J. Power Sources* **2018**, *389*, 120−134.

(9) Rangasamy, E.; Wolfenstine, J.; Sakamoto, J. The role of Al and Li concentration on the formation of cubic garnet solid electrolyte of nominal composition $Li_7La_3Zr_2O_{12}$. *Solid State Ion.* **2012**, *206*, 28−32.

(10) Li, C.; Liu, Y.; He, J.; Brinkman, K. S. Ga-substituted $Li_7La_3Zr_2O_{12}$: An investigation based on grain coarsening in garnet-type lithium ion conductors. *J. Alloys Compd.* **2017**, *695*, 3744−3752.

(11) Zhang, Y.; Chen, F.; Tu, R.; Shen, Q.; Zhang, L. Field assisted sintering of dense Al-substituted cubic phase $Li_7La_3Zr_2O_{12}$ solid electrolytes. *J. Power Sources* **2014**, *268*, 960−964.

(12) Hongahally Basappa, H. R.; Ito, T.; Morimura, T.; Bekarevich, R.; Mitsuishi, K.; Yamada. Grain boundary modification to suppress lithium penetration through garnet-type solid electrolyte. *J. Power Sources* **2017**, *363*, 145−152.

(13) Yamada, H.; Ito, T.; Hongahally Basappa, R. Sintering Mechanisms of High-Performance Garnet-type Solid Electrolyte Densified by Spark Plasma Sintering. *Electrochim. Acta* **2016**, *222*, 648−656.

(14) Afyon, S.; Krumeich, F.; Rupp, J. L. M. A shortcut to garnet-type fast Li-ion conductors for all-solid-state batteries. *J. Mater. Chem. A* **2015**, *3*, 18636−18648.

(15) Geiger, M. C. A.; Alekseev, E.; Lazic, B.; Fisch, M.; Armbruster, T.; Langner, R.; Fechtelkord, M.; Pettke, T.; Weppner, W.; Kim, N. Crystal chemistry and stability of "$Li_7La_3Zr_2O_{12}$" garnet: A fast lithium-ion conductor. *Inorg. Chem.* **2011**, *50*, 1089−1097.

(16) Klenk, M.; Lai, W. Local structure and dynamics of lithium garnet ionic conductors: tetragonal and cubic $Li_7La_3Zr_2O_{12}$. *Phys. Chem. Chem. Phys.* **2015**, *17*, 8758−8768.

(17) Song, S.; Sheptyakov, D.; Korsunsky, A. M.; Duong, H. M.; Lu, L. High Li ion conductivity in a garnet-type solid electrolyte via unusual site occupation of the doping Ca ions. *Mater. Des.* **2016**, *93*, 232−237.

(18) Rettenwander, D.; Geiger, C. A.; Amthauer, G. Synthesis and Crystal Chemistry of the Fast Li-Ion Conductor $Li_7La_3Zr_2O_{12}$ Doped with Fe. *Inorg. Chem.* **2013**, *52*, 8005−8009.

(19) Düvel, A.; Kuhn, A.; Robben, L.; Wilkening, M.; Heitjans, P. Mechanosynthesis of Solid Electrolytes: Preparation, Characterization, and Li Ion Transport Properties of Garnet-Type Al-Doped $Li_7La_3Zr_2O_{12}$ Crystallizing with Cubic Symmetry. *J. Phys. Chem. C* **2012**, *116*, 15192−15202.

(20) Kuhn, A.; Choi, J.; Robben, L.; Tietz, F.; Wilkening, M.; Heitjans, P. Li Ion Dynamics in Al-Doped Garnet-Type $Li_7La_3Zr_2O_{12}$ Crystallizing with Cubic Symmetry. *Z. Phys. Chem.* **2012**, *226*, 525−537.

(21) Gai, J.; Zhao, E.; Ma, F.; Sun, D.; Ma, X.; Jin, Y.; Wu, Q.; Cui, Y. Improving the Li-ion conductivity and air stability of cubic $Li_7La_3Zr_2O_{12}$ by the co-doping of Nb, Y on the Zr site. *J. Eur. Ceram. Soc.* **2018**, *38*, 1673−1678.

(22) Ma, X.; Xu, Y.; Zhang, B.; Xue, X.; Wang, C.; He, S.; Lin, J.; Yang, L. Garnet Si−$Li_7La_3Zr_2O_{12}$ electrolyte with a durable, low resistance interface layer for all-solid-state lithium metal batteries. *J. Power Sources* **2020**, *453*, 227881.

(23) Song, S.; Chen, B.; Ruan, Y.; Sun, J.; Yu, L.; Wang, Y.; Thokchom, J. Gd-doped $Li_7La_3Zr_2O_{12}$ garnet-type solid electrolytes for all-solid-state Li-Ion batteries. *Electrochim. Acta* **2018**, *270*, 501−508.

(24) Brugge, R. H.; Kilner, J. A.; Aguadero, A. Germanium as a donor dopant in garnet electrolytes. *Solid State Ion.* **2019**, *337*, 154−160.
(25) Liu, C.; Rui, K.; Shen, C.; Badding, M. E.; Zhang, G.; Wen, Z. Reversible ion exchange and structural stability of garnet-type Nb-doped $Li_7La_3Zr_2O_{12}$ in water for applications in lithium batteries. *J. Power Sources* **2015**, *282*, 286−293.
(26) Ji, Y.; Zhou, C.; Lin, F.; Li, B.; Yang, F.; Zhu, H.; Duan, J.; Chen, Z. Submicron-Sized Nb-Doped Lithium Garnet for High Ionic Conductivity Solid Electrolyte and Performance of Quasi-Solid-State Lithium Battery. *Materials* **2020**, *13*, 560.
(27) Adams, S.; Prasada Rao, R. Ion transport and phase transition in $Li_{7-x}La_3Zr_{2-x}M_xO_{12}$ (M = Ta^{5+}, Nb^{5+}, x = 0, 0.25). *J. Mater. Chem.* **2012**, *22*, 1426−1434.
(28) Thompson, T.; Wolfenstine, J.; Allen, J. L.; Johannes, M.; Huq, A.; David, I. N.; Sakamoto, J. Tetragonal vs. cubic phase stability in Al-free Ta doped $Li_7La_3Zr_2O_{12}$ (LLZO). *J. Mater. Chem. A* **2014**, *2*, 13431−13436.
(29) Chen, X.; Cao, T.; Xue, M.; Lv, H.; Li, B.; Zhang, C. Improved room temperature ionic conductivity of Ta and Ca doped $Li_7La_3Zr_2O_{12}$ via a modified solution method. *Solid State Ion.* **2018**, *314*, 92−97.
(30) Yang, T.; Li, Y.; Wu, W.; Cao, Z.; He, W.; Gao, Y.; Liu, J.; Li, G. The synergis-tic effect of dual substitution of Al and Sb on structure and ionic conductivity of $Li_7La_3Zr_2O_{12}$ ceramic. *Ceram. Int.* **2018**, *44*, 1538−1544.
(31) Ramakumar, S.; Satyanarayana, L.; Manorama, S. V.; Murugan, R. Structure and Li^+ dynamics of Sb-doped $Li_7La_3Zr_2O_{12}$ fast lithium ion conductors. *Phys. Chem. Chem. Phys.* **2013**, *15*, 11327−11338.
(32) Luo, Y.; Li, X.; Chen, H.; Guo, L. Influence of sintering aid on the microstructure and conductivity of the garnet-type W-doped $Li_7La_3Zr_2O_{12}$ ceramic electrolyte. *J. Mater. Sci.: Mater. Electron.* **2019**, *30*, 17195−17201.
(33) Deviannapoorani, C.; Dhivya, L.; Ramakumar, S.; Murugan, R. Lithium ion transport properties of high conductive tellurium substituted $Li_7La_3Zr_2O_{12}$ cubic lithium garnets. *J. Power Sources* **2013**, *240*, 18−25.
(34) Miara, L. J.; Richards, W. D.; Wang, Y. E.; Ceder, G. First-Principles Studies on Cation Dopants and Electrolyte Cathode Interphases for Lithium Garnets. *Chem. Mater.* **2015**, *27*, 4040−4047.
(35) Wolfenstine, J.; Allen, J. L.; Read, J.; Sakamoto, J. Chemical stability of cubic $Li_7La_3Zr_2O_{12}$ with molten lithium at elevated temperature. *J. Mater. Sci.* **2013**, *48*, 5846−5851.
(36) Zhu, Y.; Connell, J. G.; Tepavcevic, S.; Zapol, P.; Garcia-Mendez, R.; Taylor, N. J.; Sakamoto, J.; Ingram, B. J.; Curtiss, L. A.; Freeland, J. W.; Fong, D. D.; Markovic, N. M. Dopant-Dependent Stability of Garnet Solid Electrolyte Interfaces with Lithium Metal. *Adv. Energy Mater.* **2019**, *9*, 1803440.
(37) Ma, C.; Cheng, Y.; Yin, K.; Luo, J.; Sharafi, A.; Sakamoto, J.; Li, J.; More, K.; Dudney, N. J.; Chi, M. Interfacial Stability of Li Metal-Solid Electrolyte Elucidated via in Situ Electron Microscopy. *Nano Lett.* **2016**, *16*, 7030−7036.
(38) Famprikis, T.; Canepa, P.; Dawson, J. A.; Islam, M. S.; Masquelier, C. Fundamentals of inorganic solid-state electrolytes for batteries. *Nat. Mater.* **2019**, *18*, 1278−1291.
(39) Nemori, H.; Matsuda, Y.; Mitsuoka, S.; Matsui, M.; Yamamoto, O.; Takeda, Y.; Imanishi, N. Stability of garnet-type solid electrolyte $Li_xLa_3A_{2-y}$ (A = Nb or Ta, B= Sc or Zr). *Solid State Ion.* **2015**, *282*, 7−12.
(40) Rettenwander, D.; Wagner, R.; Reyer, A.; Bonta, M.; Cheng, L.; Doeff, M. M.; Limbeck, A.; Wilkening, M.; Amthauer, G. Interface Instability of Fe-Stabilized $Li_7La_3Zr_2O_{12}$ versus Li metal. *J. Phys. Chem. C* **2018**, *122*, 3780−3785.
(41) Zhu, J.; Li, X.; Wu, C.; Gao, J.; Xu, H.; Li, Y.; Guo, X.; Li, H.; Zhou, W. A Multilayer Ceramic Electrolyte for All-Solid-State Li Batteries. *Angew.* **2021**, *60*, 3781−3790.
(42) Thompson, T.; Sharafi, A.; Johannes, M. D.; Huq, A.; Allen, J. L.; Wolfenstine, J.; Sakamoto, J. A Tale of Two Sites: On Defining the Carrier Concentration in Garnet-Based Ionic Conductors for Advanced Li Batteries. *Adv. Energy Mater.* **2015**, *5*, 1500096.
(43) Kim, Y.; Yoo, A.; Schmidt, R.; Sharafi, A.; Lee, H.; Wolfenstine, J.; Sakamoto, J. Electrochemical Stability of $Li_{6.5}La_3Zr_{1.5}M_{0.5}O_{12}$ (M = Nb or Ta) against Metallic Lithium. *Front. Energy Res.* **2016**, *4*, 20.
(44) Ishiguro, K.; Nakata, Y.; Matsui, M.; Uechi, I.; Takeda, Y.; Yamamoto, O.; Imanishi, N. Stability of Nb-Doped $Li_7La_3Zr_2O_{12}$ with Lithium Metal. *J. Electrochem. Soc.* **2013**, *160*, A1690−A1693.
(45) Fu, K.; Gong, Y.; Liu, B.; Zhu, Y.; Xu, S.; Yao, Y.; Luo, W.; Wang, C.; Lacey, S. D.; Dai, J.; Chen, Y.; Mo, Y.; Wachsman, E.; Hu, L. Toward garnet electrolyte−based Li metal batteries: An ultrathin, highly effective, artificial solid-state electrolyte/metallic Li interface. *Sci. Adv.* **2017**, *3*, 1−12.
(46) Han, X.; Gong, Y.; Fu, K.; He, X.; Hitz, G. T.; Dai, J.; Pearse, A.; Liu, B.; Wang, H.; Rubloff, G.; Mo, Y.; Thangadurai, V.; Wachsman, E. D.; Hu, L. Negating interfacial impedance in garnet-based solid-state Li metal batteries. *Nat. Mater.* **2017**, *16*, 572−579.
(47) Luo, W.; Gong, Y.; Zhu, Y.; Li, Y.; Yao, Y.; Zhang, Y.; Fu, K.; Pastel, G.; Lin, C.; Mo, Y.; Wachsman, E. D.; Hu, L. Reducing Interfacial Resistance between Garnet-Structured Solid-State Electrolyte and Li-Metal Anode by a Germanium Layer. *Adv. Mater.* **2017**, *29*, 1606042.
(48) Tsai, C. L.; Roddatis, V.; Chandran, C. V.; Ma, Q.; Uhlenbruck, S.; Bram, M.; Heitjans, P.; Guillon, O. $Li_7La_3Zr_2O_{12}$ Interface Modification for Li Dendrite Prevention. *ACS Appl. Mater. Interfaces* **2016**, *8*, 10617−10626.
(49) Shao, Y.; Wang, H.; Gong, Z.; Wang, D.; Zheng, B.; Zhu, J.; Lu, Y.; Hu, Y. S.; Li, H.; Huang, X.; Yang, Y.; Nan, C. W.; Chen, L.; Guo, X. Drawing a soft interface: An effective interfacial modification strategy for garnet-type solid-state Li batteries. *ACS Energy Lett.* **2018**, *3*, 1212−1218.
(50) Feng, W.; Dong, X.; Zhang, X.; Lai, Z.; Li, P.; Wang, C.; Wang, Y.; Xia, Y. Li/Garnet Interface Stabilization by Thermal-Decomposition Vapor Deposition of an Amorphous Carbon Layer. *Angew. Chem., Int. Ed.* **2020**, *59*, 5346−5349.
(51) Amores, M.; El-Shinawi, H.; McClelland, I.; Yeandel, S. R.; Baker, P. J.; Smith, R. I.; Playford, H. Y.; Goddard, P.; Cussen, E. J.; Corr, S. A. $Li_{1.5}La_{1.5}MO_6$ (M = W^{6+}, Te^{6+}) as a new series of lithium-rich double perovskites for all-solid-state lithium-ion batteries. *Nat. Commun.* **2020**, *11*, 6392.
(52) Momma, K.; Izumi, F. VESTA 3 for three-dimensional visualization of crystal, volumetric and morphology data. *J. Appl. Crystallogr.* **2011**, *44*, 1272−1276.
(53) Arnold, O.; Bilheux, J. C.; Borreguero, J. M.; Buts, A.; Campbell, S. I.; Chapon, L.; Doucet, M.; Draper, N.; Ferraz Leal, R.; Gigg, M. A.; Lynch, V. E.; Markvardsen, A.; Mikkelson, D. J.; Mikkelson, R. L.; Miller, R.; Palmen, K.; Parker, P.; Passos, G.; Perring, T. G.; Peterson, P. F.; Ren, S.; Reuter, M. A.; Savici, A. T.; Taylor, J. W.; Taylor, R. J.; Tolchenov, R.; Zhou, W.; Zikovsky, J. Nuclear Instruments and Methods in Physics Research Section A: Accelerators, Spectrometers, Detectors and Associated Equipment. *Nucl. Instrum. Meth. A* **2014**, *764*, 156−166.
(54) Ravel, B.; Newville, M. ATHENA, ARTEMIS, HEPHAESTUS: data analysis for X-ray absorption spectroscopy using IFEFFIT. *J. Synchrotron Rad.* **2005**, *12*, 537−541.
(55) Irvine, J. T. S.; Sinclair, D. C.; West, A. R. Electroceramics: Characterization by Impedance Spectroscopy. *Adv. Mater.* **1990**, *2*, 132−138.
(56) El-Shinawi, H.; Paterson, G. W.; MacLaren, D. A.; Cussen, E. J.; Corr, S. A. Low-temperature densification of Al-doped $Li_7La_3Zr_2O_{12}$″ a reliable and controllable synthesis of fast-ion conducting garnets. *J. Mater. Chem. A* **2017**, *5*, 319−329.
(57) Xie, H.; Park, K.; Song, J.; Goodenough, J. B. Reversible lithium insertion in the garnet framework of $Li_3Nd_3W_2O_{12}$. *Electrochem. Commun.* **2012**, *19*, 135−137.
(58) Satish, R.; Aravindan, V.; Ling, W. C.; Goodenough, J. B.; Madhavi, S. Carbon-Coated $Li_3Nd_3W_2O_{12}$: A High Power and Low-Voltage Insertion Anode with Exceptional Cycleability for Li-Ion Batteries. *Adv. Energy. Mater.* **2014**, *4*, 1301715.

https://doi.org/10.1021/acs.chemmater.2c00379
Chem. Mater. 2022, 34, 5054−5064

(59) Luo, M.; Yu, H.; Cheng, X.; Ye, W.; Zhu, H.; Liu, T.; Peng, N.; Shui, M.; Shu, J. Sol-Gel Synthesis and in Situ X-ray Diffraction Study of $Li_3Nd_3W_2O_{12}$ as a Lithium Container. *ACS. Appl. Mater. Interfaces* **2018**, *10*, 12716−12721.
(60) Sharafi, A.; Meyer, H. M.; Nanda, J.; Wolfenstine, J.; Sakamoto, J. Characterizing the li-$Li_7La_3Zr_2O_{12}$ interface stability and kinetics as a function of temperature and current density. *J. Power Sources* **2016**, *302*, 135−139.
(61) McClelland, I.; Johnston, B.; Baker, P. J.; Amores, M.; Cussen, E. J.; Corr, S. A. Muon Spectroscopy for Investigating Diffusion in Energy Storage Materials. *Annu. Rev. Mater. Res.* **2020**, *50*, 371.
(62) Blundell, S. J. Spin-polarized muons in condensed matter physics. *Contemporary Physics* **1999**, *40*, 175−192.
(63) Sugiyama, J.; Nozaki, H.; Umegaki, I.; Mukai, K.; Miwa, K.; Shiraki, S.; Hitosugi, T.; Suter, A.; Prokscha, T.; Salman, Z.; Lord, J. S.; Månsson, M. Li-ion diffusion in $Li_4Ti_5O_{12}$ and $LiTi_2O_4$ battery materials detected by muon spin spectroscopy. *Phys. Rev. B* **2015**, *92*, 014417.
(64) Buschmann, H.; Dölle, J.; Berendts, S.; Kuhn, A.; Bottke, P.; Wilkening, M.; Heitjans, P.; Senyshyn, A.; Ehrenberg, H.; Lotnyk, A.; Duppel, V.; Kienle, L.; Janek, J. Structure and dynamics of the fast lithium ion conductor "$Li_7La_3Zr_2O_{12}$". *Phys. Chem. Chem. Phys.* **2011**, *13*, 19378−19392.
(65) Dalmas De Réotier, P.; Yaouanc, A. Muon spin rotation and relaxation in magnetic materials. *J. Phys.: Condens. Matter* **1997**, *9*, 9113−9166.
(66) Stone, N. J. Table of nuclear magnetic dipole and electric quadrupole moments. *At. Data Nucl. Data Tables* **2005**, *90*, 75−176.
(67) Brewer, J. H.; Crowe, K. M.; Gygax, F. N.; Johnson, R. F.; Patterson, B. D.; Fleming, D. G.; Schenck, A. Anomalous μ^+ Precession in Silicon. *Phys. Rev. Lett.* **1973**, *31*, 143−146.
(68) Blundell, S. J. Muon-spin rotation studies of electronic properties of molecular conductors and superconductors. *Chem. Rev.* **2004**, *104*, 5717−5735.
(69) Sugiyama, J.; Nozaki, H.; Umegaki, I.; Mukai, K.; Cottrell, S. P.; Shiraki, S.; Hitosugi, T.; Sassa, Y.; Suter, A.; Salman, Z.; Prokscha, T.; Månsson, M. μ^+SR Study on Li Ionic Conductors. *JPS Conf. Proc.* **2018**, *21*, 14−17.
(70) Cox, S. F. J.; Davis, E. A.; Cottrell, S. P.; King, P. J. C.; Lord, J. S.; Gil, J. M.; Alberto, H. V.; Vilao, R. C.; Piroto Duarte, J.; Ayres de Campos, N.; Weidinger, A.; Lichti, R. L.; Irvine, S. J. C. Experimental Confirmation of the Predicted Shallow Donor Hydrogen State in Zinc Oxide. *Phys. Rev. Lett.* **2001**, *86*, 2601−2604.
(71) Cox, S. F. J. Implanted muon studies in condensed matter science. *J. Phys. C: Solid state Phys.* **1987**, *20*, 3187−3319.
(72) Hayano, R. S.; Uemura, Y. J.; Imazato, J.; Nishida, N.; Yamazaki, T.; Kubo, R. Zero- and low-field spin relaxation studied by positive muons. *Phys. Rev. B* **1979**, *20*, 850−859.
(73) Månsson, M.; Sugiyama, J. Muon-spin relaxation study on Li- and Na-diffusion in solids. *Phys. Scr.* **2013**, *88*, 068509.
(74) Sugiyama, J.; Mukai, K.; Ikedo, Y.; Nozaki, H.; Månsson, M.; Watanabe, I. Li diffusion in Li_xCoO_2 probed by Muon-Spin spectroscopy. *Phys. Rev. Lett.* **2009**, *103*, 147601.
(75) Ashton, T. E.; Baker, P. J.; Bauer, D.; Groves, A. R.; Sotelo-Vazquez, C.; Kamiyama, T.; Matsukawa, T.; Kojima, K. M.; Darr, J. A. Multiple diffusion pathways in $Li_xNi_{0.77}Co_{0.14}Al_{0.09}O_2$ (NCA) Li-ion battery cathodes. *J. Mater. Chem. A* **2020**, *8*, 11545−11552.
(76) Ashton, T. E.; Laveda, J. V.; Maclaren, D. A.; Baker, P. J.; Porch, A.; Jones, M. O.; Corr, S. A. Muon studies of Li^+ diffusion in $LiFePO_4$ nanoparticles of different polymorphs. *J. Mater. Chem. A* **2014**, *2*, 6238−6245.
(77) Laveda, J. V.; Johnston, B.; Paterson, G. W.; Baker, P. J.; Tucker, M. G.; Playford, H. Y.; Jensen, K. M. Ø.; Billinge, S. J. L.; Corr, S. A. Structure-property insights into nanostructured electrodes for Li-ion batteries from local structural and diffusional probes. *J. Mater. Chem. A* **2018**, *6*, 127−137.
(78) Nozaki, H.; Harada, M.; Ohta, S.; Watanabe, I.; Miyake, Y.; Ikedo, Y.; Jalarvo, N. H.; Mamontov, E.; Sugiyama, J. Li diffusive behavior of garnet-type oxides studied by muon-spin relaxation and QENS. *Solid State Ion.* **2014**, *262*, 585−588.
(79) Awaka, J.; Kijima, N.; Hayakawa, H.; Akimoto, J. Synthesis and structure analysis of tetragonal $Li_7La_3Zr_2O_{12}$ with the garnet-related type structure. *J. Solid State Chem.* **2009**, *182*, 2046−2052.
(80) Balerna, A.; Bernieri, E.; Burattini, E.; et al. XANES studies of MeO_{3-x} (Me = W, Re, Ir) crystalline and amorphous oxides. *Nucl. Instrum. Methods. Phys. Res. A* **1991**, *308*, 240−242.
(81) Flatscher, F.; Philipp, M.; Ganschow, S.; Wilkening, H. M. R.; Rettenwander, D. The natural critical current density limit for $Li_7La_3Zr_2O_{12}$ garnets. *J. Mater. Chem. A* **2020**, *8*, 15782−15788.
(82) Yamazoe, S.; Hitomi, Y.; Shishido, T.; Tanaka, T. XAFS Study of Tungsten L1-and L3-Edges: Structural Analysis of WO_3 Species Loaded on TiO_2 as a Catalyst for Photo-oxidation of NH_3. *J. Phys. Chem. C* **2008**, *112*, 6869−6879.
(83) Jayarathne, U.; Chandrasekaran, P.; Greene, A. F.; Mague, J. T.; DeBeer, S.; Lancaster, K. M.; Sproules, S.; Donahue, J. P. X-ray Absorption Spectroscopy Systematics at the Tungsten L-Edge. *Inorg. Chem.* **2014**, *53*, 8230−8241.

https://doi.org/10.1021/acs.chemmater.2c00379
Chem. Mater. 2022, 34, 5054−5064